AIP Advances

TEM and electron diffraction analysis of ω-Fe to cementite transformation in quenched and tempered high carbon steels

Cite as: AIP Advances **9**, 045219 (2019); https://doi.org/10.1063/1.5091847
Submitted: 06 February 2019 . Accepted: 08 April 2019 . Published Online: 18 April 2019

Tianwei Liu, Tong Li, and Xingfa Liu

TEM and electron diffraction analysis of ω-Fe to cementite transformation in quenched and tempered high carbon steels

Cite as: AIP Advances 9, 045219 (2019); doi: 10.1063/1.5091847
Submitted: 6 February 2019 • Accepted: 8 April 2019 •
Published Online: 18 April 2019

Tianwei Liu,[a] Tong Li,[b] and Xingfa Liu[c]

AFFILIATIONS

State Key Laboratory of Nonlinear Mechanics, Institute of Mechanics, Chinese Academy of Sciences, Beijing 100190, China

[a]Corresponding author: liutianwei@lnm.imech.ac.cn
[b]litong@lnm.imech.ac.cn
[c]liuxingfa@lnm.imech.ac.cn

ABSTRACT

Quenching and tempering are mostly employed to tune the mechanical properties of the high-carbon steels. In the present study, transmission electron microscopy (TEM) and selected area electron diffraction (SAED) are used to examine the microstructural evolution in quenched and tempered high carbon steels. In quenched specimens, the ω-Fe(C) phase is a common substructure in twinned martensite and its diffraction spots are located at 1/3 and 2/3 $(2\bar{1}1)_{\alpha\text{-Fe}}$ positions along the $[011]_{\alpha\text{-Fe}}$ zone axis (ZA). When specimens are *in-situ* heated in TEM, few additional diffraction spots are observed at 1/6, 3/6 and 5/6 $(2\bar{1}1)_{\alpha\text{-Fe}}$ positions along the $[011]_{\alpha\text{-Fe}}$ ZA. Moreover, martensite decomposes into a lamellar structure and ω-Fe(C) phase transforms into θ-Fe_3C cementite during tempering. The TEM and electron diffraction analysis reveals that diffraction spots of θ-Fe_3C cementite phase are located at 1/6, 2/6, 3/6, 4/6 and 5/6 $(22\bar{2})_{\alpha\text{-Fe}}$ and $(2\bar{1}1)_{\alpha\text{-Fe}}$ along $[112]_{\alpha\text{-Fe}}$ and $[011]_{\alpha\text{-Fe}}$ ZAs. Furthermore, the orientation relationships between θ-Fe_3C cementite and α-Fe are indexed as: $[013]_\theta//[112]_{\alpha\text{-Fe}}$, $[001]_\theta//[011]_{\alpha\text{-Fe}}$, $[\bar{1}13]_\theta//[111]_{\alpha\text{-Fe}}$ and $[\bar{1}02]_\theta//[131]_{\alpha\text{-Fe}}$, which are related to the transformation of ω-Fe to θ-Fe_3C cementite. The current study provides a baseline to understand the microstructural evolution in high carbon steels during heat treatment processes.

I. INTRODUCTION

Quenched high carbon steel renders excellent strength but suffers from high brittleness. In general, heat treatments, such as tempering or aging, are carried out to obtain a desirable combination of strength and toughness.[1–3] The strength of steel generally decreases, whereas the toughness increases, with increasing tempering temperature and time. Lots of studies have reported different heat-treatment processes and tempering parameters.[4–6] Usually, a highly complex microstructural evolution occurs in quenched martensite during tempering, including the formation of fine carbides, the decomposition of retained austenite and the nucleation and growth of cementite.[7–12] The type and morphology of carbides play a critical role in determining the structural characteristics and mechanical properties of tempered steels.[13–15]

In high carbon steels, twins are usually observed as the substructure of martensite.[16–18] Earlier transmission electron microscopy (TEM) observations have revealed that carbides are significantly influenced by the presence of fine twins. Most of the carbides prefer to nucleate and precipitate on twinning planes instead of other kinds of boundaries or dislocations in tempered carbon steels.[19,20] Moreover, cementite is usually aligned along the $\langle 111\rangle_{\alpha\text{-Fe}}$ directions on the $\{112\}_{\alpha\text{-Fe}}$ twinning planes.[19,20] Recently, a metastable ω-Fe phase, which is a common substructure in steels, has been unambiguously revealed by systematical electron diffraction analysis.[21–25] The fine particle-like ω-Fe phase coexists with $\{112\}\langle 111\rangle$-type body-centered cubic (bcc) twin boundaries in a twinned martensite structure.[22–25] In carbon steels, carbon atoms occupy the octahedral interstitial sites in ω-Fe phase and stabilize fine particle-like ω-Fe phase.[11,12,22–25] During tempering, the ω-Fe phase could transform into θ-Fe_3C cementite.[11,12,25]

However, detailed investigation and further understanding of the correlation between ω phase and carbides (cementite) in tempered martensite is required due to the importance of martensitic substructure and carbides. Herein, we have carried out detailed TEM and electron diffraction analysis of martensite during tempering of water-quenched Fe-1.4C (wt. %) binary alloy.

II. EXPERIMENTAL PROCEDURE

An Fe-1.4C (1.4 wt. % carbon) ingot was prepared in a high vacuum induction furnace under argon atmosphere. The ingot was solution treated at ~1200 °C for 2 h and, subsequently, hot forged into a thick plate. A 20 mm × 20 mm × 1.5 mm plate was mechanically sectioned and austenitized at 950 °C for 30 min, followed by water quenching (~150 °C/s). Some of the quenched specimens were tempered at 200 °C and 400 °C for 30 min. Phase identification was carried out by using an X-ray diffraction (XRD) diffractometer (Rigaku SMARTLAB), equipped with Cu-Kα radiations and operated at 45 kV and 200 mA. TEM specimens were mechanically ground, polished and ion-milled (Gatan PIPS II 695) at room temperature. The microstructure was characterized using JEM 2100 and 2100F TEM, operating at 200 kV. The heating rate of in-situ TEM observations was ~20 °C/min. The electron diffraction analysis was performed using by Crystal-Maker (CrystalMaker Software Ltd).

III. RESULTS

A. Morphology and crystallography of as-quenched martensite

Fig. 1 presents the crystallography and morphology of a water-quenched Fe-1.4C specimen, austenitized at 950 °C for 30 min. Fig. 1(a) shows the XRD pattern of the quenched specimen, which indicates that martensite and retained austenite are the primary constituents of the specimen. Fig. 1(b) shows a bright-field TEM image of the quenched specimen, which also confirmed the presence of two phases, martensite and retained austenite. The martensite phase exhibits a plate-like morphology, whereas the retained austenite can be identified from the dislocation contrast close to the martensite. In high carbon steel, twins represent a common substructure in martensite.[16–18] Due to the diffraction conditions, the twin contrast of some martensite in Fig. 1(b) cannot be seen. Fig. 1(c) shows the bright-field TEM image of individual martensite structure without twin contrast. By tilting the specimen, different diffraction contrasts of the martensite have been obtained, as shown in Figs. 1(d) and 1(e). Moreover, the martensite in Fig. 1(d) exhibits an obvious twin contrast compared to Fig. 1(c).

Fig. 2 presents further TEM observations of twinned martensite structure, as shown in Fig. 1(d). Figs. 2(a) and 2(b) show a bright-field TEM image of twinned martensite and corresponding selected area electron diffraction (SAED) pattern along $[011]_{\alpha\text{-Fe}}$ zone axis (ZA), respectively. Apart from α-Fe diffraction spots, two extra diffraction spots at the 1/3 and 2/3$(2\bar{1}1)_{\alpha\text{-Fe}}$ positions are presented in Fig. 2(b). These extra diffraction spots are often observed in martensite and have been confirmed to originate from ω-Fe phase.[21–25] Figs. 2(c) and 2(d) present the dark-field TEM images, which are obtained by using twin $(0\bar{1}1)_t$ and ω-Fe $(0\bar{1}10)_\omega$ diffraction spots in Fig. 2(b), respectively. Fig. 2(f) shows an enlarged dark-field TEM image of the region, outlined by dashed-line frame in Fig. 2(d). Fig. 2(g) shows a high-resolution TEM (HRTEM) lattice image of the twinned martensite. The corresponding Fourier-filtered transformed (FFT) diffraction pattern and the inversed FFT lattice image of Fig. 2(g) are shown in Figs. 2(h) and 2(i), respectively. The dark-field image (Fig. 2(c)) and HRTEM lattice image (Fig. 2(g)) reveal the twin contrast and indicate that most of the twins are several to dozens of nanometers in thickness. The ω-Fe phase is located at the

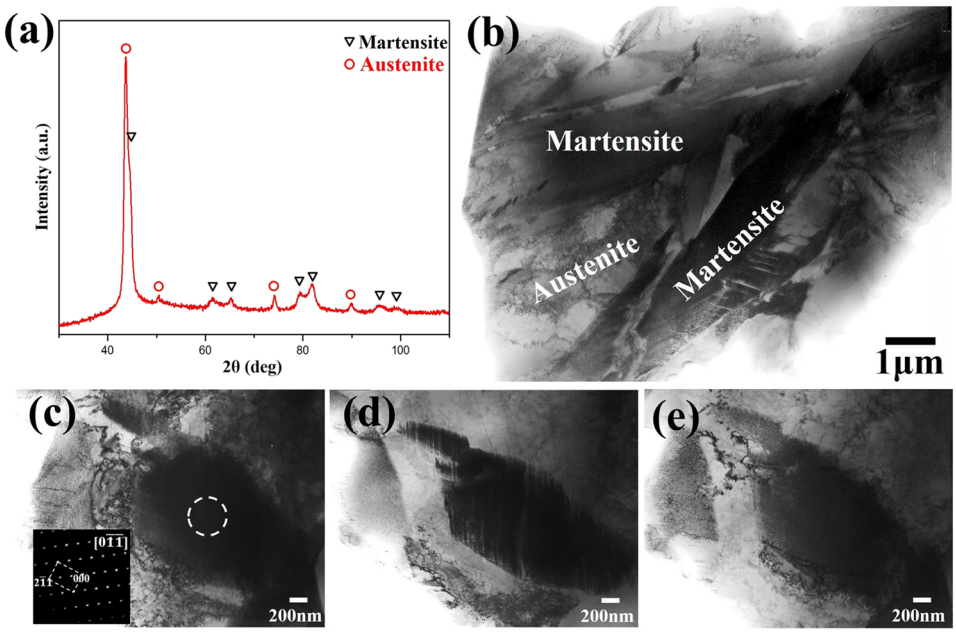

FIG. 1. (a) XRD pattern and (b) bright-field TEM image of a quenched Fe-1.4C (wt. %) specimen; (c) a martensite and (inset) corresponding SAED pattern without twin contrast; (d) and (e) bright-field TEM images of the martensite shown in (c) after tilting.

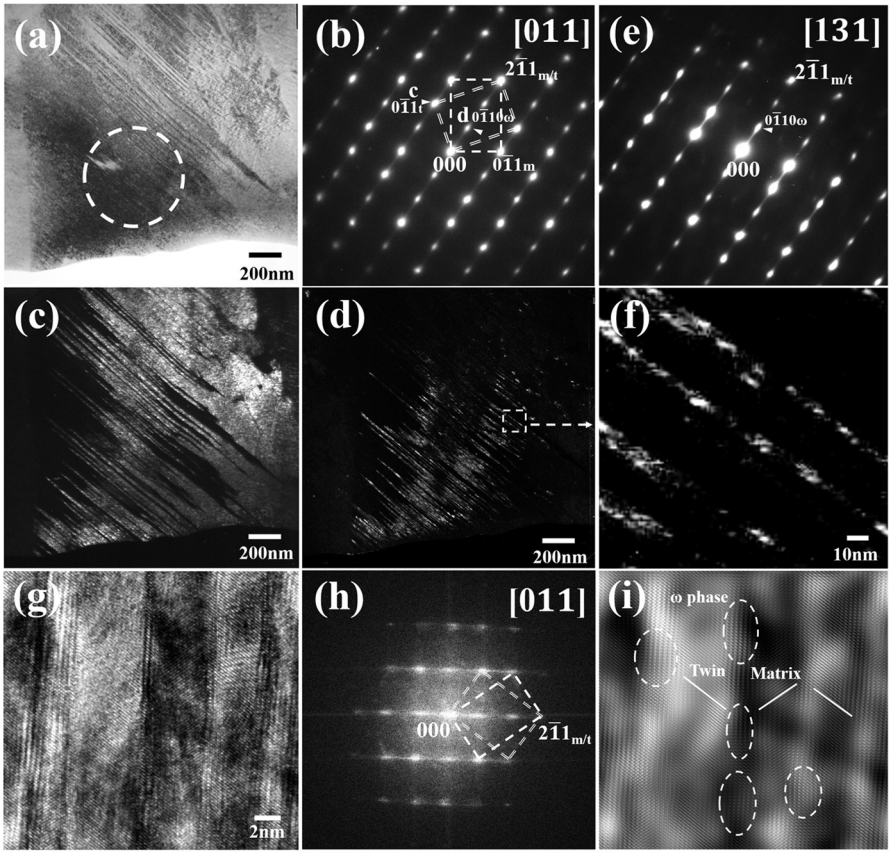

FIG. 2. (a) a bright-field TEM image of twinned martensite in the quenched Fe-1.4C (wt. %) specimen; (b) the corresponding SAED pattern of martensite along [011] $_{\alpha\text{-Fe}}$ ZA, obtained from the dashed circle in (a); (c) and (d) dark-field TEM images of diffraction spots "*c*" and "*d*" in (b), respectively; (e) the corresponding SAED pattern along $[131]_{\alpha\text{-Fe}}$ ZA by tilting from (b); (f) an enlarged dark-field TEM image from the dashed-line frame, outlined in (d); (g) a high-resolution TEM lattice image of twinned martensite; (h) the Fourier-filtered transformed (FFT) diffraction pattern of (g); (i) the Inverse FFT image of (g) displaying an HRTEM image with bcc twin and ω-Fe lattice. The subscripts 'm' and 't' denote matrix crystal and twin crystal, respectively.

twin boundary region and exhibits an ultra-fine particle-like contrast and morphology (Figs. 2(f) and 2(i)). The SAED pattern in Fig. 2(e) was taken along $[131]_{\alpha\text{-Fe}}$ ZA by tilting 31.5° from Fig. 2(b) and the extra diffraction spots are still observed at 1/3 and 2/3 $(2\bar{1}1)_{\alpha\text{-Fe}}$ positions.

B. Evolution of martensite during tempering

Martensite decomposes during tempering of the quenched specimen and ω-Fe phase transforms into carbides or cementite.[11,12,25] In order to determine the transformation process associated with the ω-Fe phase, *in-situ* TEM observations were carried out during heating at a heating rate of 20 °C/min. Fig. 3 presents TEM images of quenched Fe-1.4C specimen, gathered during *in-situ* heating. Fig. 3(a) displays a bright-field TEM image of martensite at room temperature. Fig. 3(d) shows the corresponding SAED pattern of the martensite, obtained from the marked area in Fig. 3(a). The additional diffraction spots at 1/3 and 2/3 $(2\bar{1}1)_{\alpha\text{-Fe}}$ positions, along $[011]_{\alpha\text{-Fe}}$ ZA, indicate the presence of ω-Fe phase in martensite. Figs. 3(b) and 3(c) show bright-field TEM images of the specimen heated at 250 °C and 350 °C. The holding time at each temperature was 10 min. The corresponding SAED patterns of the heated sample are presented in Figs. 3(e) and 3(f), respectively. The martensite decomposed into a lamellar structure after heating at 250 °C. In addition, some new diffraction spots emerged at 1/6, 3/6 and 5/6 $(2\bar{1}1)_{\alpha\text{-Fe}}$ positions in Fig. 3(e), which are not present in SAED pattern given in Fig. 3(d). However, the intensity of these new diffraction spots is weaker than the spots at 1/3 and 2/3 $(2\bar{1}1)_{\alpha\text{-Fe}}$. It is worth mentioning that the carbide (cementite) became coarser at 350 °C than that at 250 °C (Figs. 3(b) and (c)). Meanwhile, the difference in diffraction intensity between the extra diffraction spots became smaller due to the formation and coarsening process of the carbides (cementite) (Figs. 3(e) and (f)).

In order to demonstrate the generalized nature of the above phenomenon, TEM observations of the quenched specimens, tempered at 200 °C and 400 °C for 30 minutes, were carried out and results are presented in Fig. 4. Figs. 4(a) and 4(b) show the morphology and corresponding SAED pattern of martensite after tempering at 200°C, which are similar to those in Figs. 3(b) and 3(e). After tilting the ZA from $[011]_{\alpha\text{-Fe}}$ to $[131]_{\alpha\text{-Fe}}$, the 1/6, 3/6, and 5/6 $(2\bar{1}1)_{\alpha\text{-Fe}}$ diffraction spots are also observed to be weaker than the 1/3 and 2/3 $(2\bar{1}1)_{\alpha\text{-Fe}}$ spots (Fig. 4(c)), which implies that the extra diffraction spots originated from a unified carbide (cementite). Figs. 4(d–f) show the bright-field TEM image and corresponding SAED pattern of the quenched specimen after tempering at 400 °C. The TEM image exhibited an obvious lamellar structure (Fig. 4(d)), however, the extra diffraction spots did not exhibit any significant difference in intensity (Figs. 4(e) and 4(f)).

To further investigate the structural changes and formation of the carbide (cementite) during tempering, TEM images and SAED

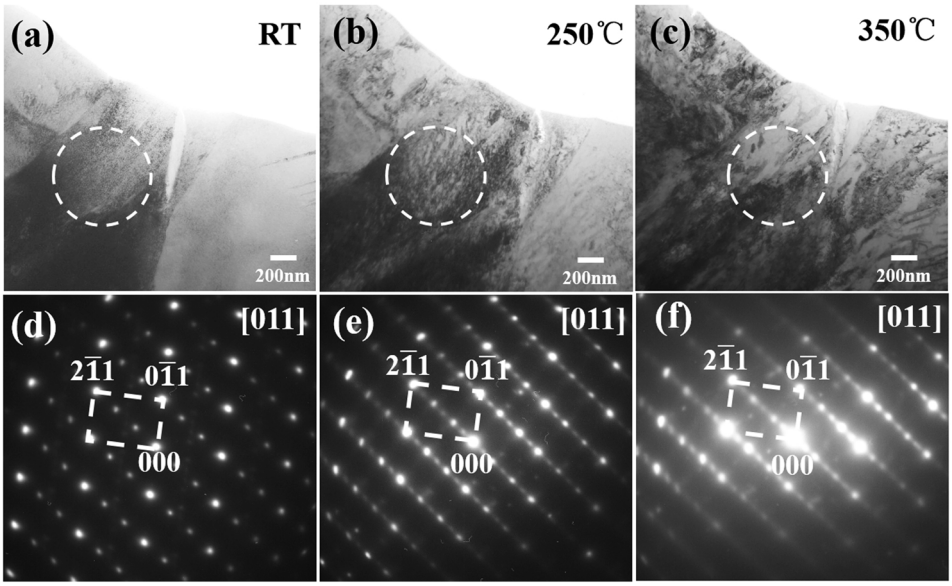

FIG. 3. *In-situ* TEM images of the as-quenched Fe-1.4C specimen during heating.

patterns were obtained from tempered martensite at various tilt angles. Figs. 5(a) and 5(b) present a bright-field TEM image and corresponding SAED of the tempered specimen, which is shown in Fig. 4(d). The SAED pattern was obtained from the marked area in Fig. 5(a). Two sets of diffraction spots are clearly visible in the SAED pattern along the $[112]_{\alpha\text{-Fe}}$ ZA. The diffraction spots other than α-Fe spots are located at 1/6, 2/6, 3/6, 4/6 and 5/6 $(22\bar{2})_{\alpha\text{-Fe}}$ positions. Moreover, the dark-field TEM images, presented in Figs. 5(c) and 5(d), were obtained from spots "*c*" and "*d*" in Fig. 5(b), offering more information about the carbide (cementite). Figs. 5(c) and 5(d) exhibit the needle-shaped bright lamella structure, arranged along the $[11\bar{1}]_{\alpha\text{-Fe}}$ direction. Different SAED patterns could be obtained by tilting from $[112]_{\alpha\text{-Fe}}$ ZA to $[011]_{\alpha\text{-Fe}}$, $[111]_{\alpha\text{-Fe}}$, and $[131]_{\alpha\text{-Fe}}$ ZAs as shown in Figs. 5(e–g), respectively. The additional diffraction spots are located at 1/6, 2/6, 3/6, 4/6 and 5/6 $(2\bar{1}1)_{\alpha\text{-Fe}}$ positions along $[011]_{\alpha\text{-Fe}}$ and $[131]_{\alpha\text{-Fe}}$ ZAs are shown in Fig. 5(e) and 5(g), while one spot is located at 1/2 $(2\bar{1}\bar{1})_{\alpha\text{-Fe}}$ along $[111]_{\alpha\text{-Fe}}$ ZA in Fig. 5(f). The additional diffraction spots should correspond to θ-Fe_3C cementite on the basis of chemical composition, tempering temperature and tempering time. Moreover, some of diffraction patterns are consistent with the TEM observations made in the case of θ-Fe_3C cementite, as reported previously.[9,26]

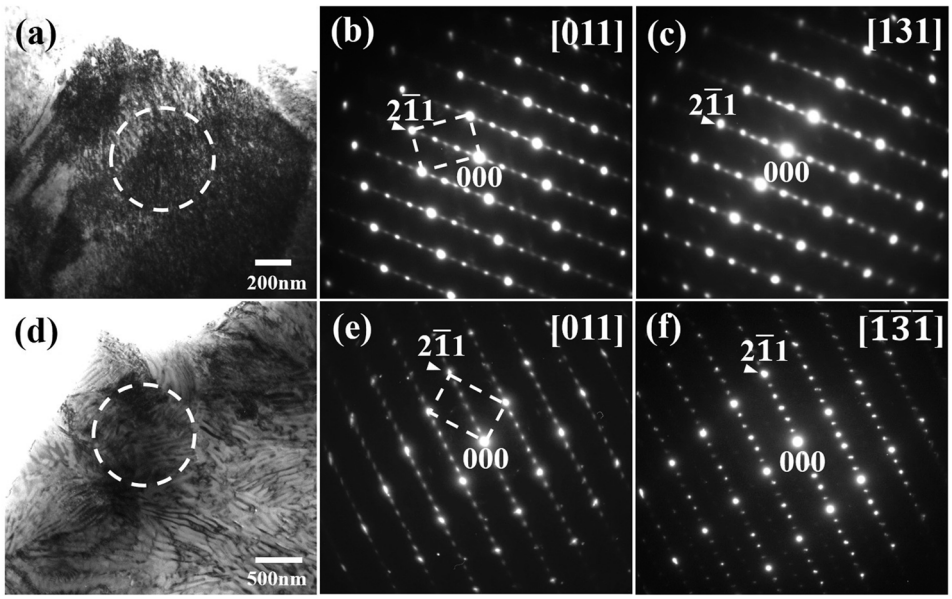

FIG. 4. Bright-field TEM images and corresponding SAED patterns of the quenched specimen after tempering at (a-c) 200 °C and (d-f) 400 °C.

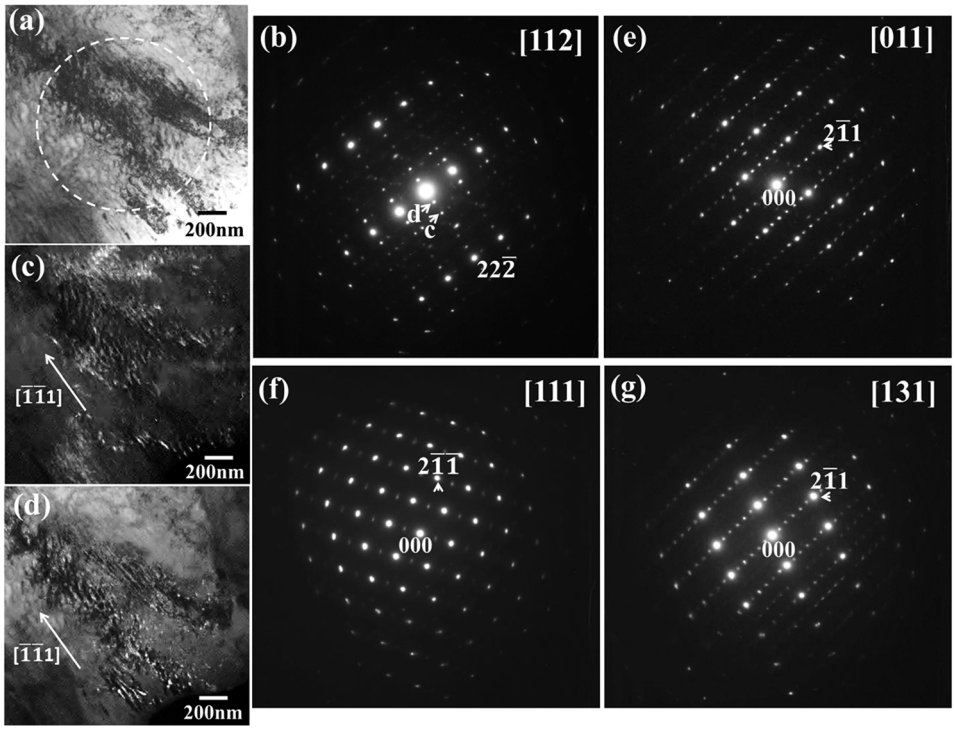

FIG. 5. (a) Bright-field TEM image of the tempered specimen; (b) SAED pattern taken along $[112]_{\alpha\text{-Fe}}$ ZA from the circle outlined in (a); (c) and (d) dark-field TEM images obtained from the diffraction spots "*c*" and "*d*" in (b); and (e-g) SAED patterns along $[011]_{\alpha\text{-Fe}}$, $[111]_{\alpha\text{-Fe}}$, and $[131]_{\alpha\text{-Fe}}$ ZAs by tilting from $[112]_{\alpha\text{-Fe}}$, respectively.

IV. DISCUSSION

We have carried out a detailed electron diffraction analysis to confirm the formation of θ-Fe_3C cementite and determine its orientation relationship (OR) with ferrite (α-Fe), as shown in Fig. 5. The lattice parameter of ferrite is a = 0.28665 nm, with the space group of $Im\bar{3}m$ (No. 229).[27] The θ-Fe_3C cementite phase has a complex orthorhombic structure with 12 iron atoms and 4 carbon atoms in one unit cell, which belongs to the space group of Pnma (No.62). The detailed structural information of the cementite phase is presented in Table I.[28,29]

Figs. 6(a–d) present the calculated electron diffraction patterns of α-Fe along $[112]_{\alpha\text{-Fe}}$, $[011]_{\alpha\text{-Fe}}$, $[111]_{\alpha\text{-Fe}}$, and $[131]_{\alpha\text{-Fe}}$ ZAs, respectively. Fig. 6(e) shows the calculated diffraction pattern of θ-Fe_3C cementite along $[013]_\theta$ ZA. The distance between $(03\bar{1})_\theta$ and $(63\bar{1})_\theta$ diffraction spots in Fig. 6(e) are nearly the same as the distance between $(\bar{1}10)_{\alpha\text{-Fe}}$ and $(13\bar{2})_{\alpha\text{-Fe}}$ spots in Fig. 6(a). In addition, five equally spaced diffraction spots between $(03\bar{1})_\theta$ and $(63\bar{1})_\theta$ spots are shown in Fig. 6(e). Figs. 6(a) and 6(e) confirm that the position of $(200)_\theta$ diffraction spot, belonging to cementite phase, overlaps with 2/6 $(22\bar{2})_{\alpha\text{-Fe}}$ spot in Fig. 5(b). However, 1/6, 3/6 and 5/6 $(22\bar{2})_{\alpha\text{-Fe}}$ spots in Fig. 5(b) cannot be simulated only from the diffraction spots of θ-Fe_3C cementite, which arise due to double diffraction between θ-Fe_3C cementite and α-Fe. In an experimental diffraction situation, the diffracted beam from α-Fe can act as the incident beam in cementite, resulting in double diffraction.[30,31] If $(1\bar{1}0)$ diffraction beam from α-Fe becomes the incident beam in cementite, the diffraction spots from cementite should combine and form an extra $[1\bar{1}0]^*_{\alpha-Fe}$ reciprocal vector.[30,31] Therefore, the diffraction spots between $(03\bar{1})_\theta$ and $(63\bar{1})_\theta$ in Fig. 6(e) were located between $(000)_{\alpha\text{-Fe}}$ and $(22\bar{2})_{\alpha\text{-Fe}}$ in Fig. 6(i). Considering the existence of double diffraction, the calculated diffraction pattern of the tempered martensite, shown in Fig. 6(i), matches well with TEM results, which are presented in Fig. 5(b). The orientation relationship (OR) between cementite and α-Fe in Fig. 5(b) can be indexed as $[013]_\theta//[112]_{\alpha\text{-Fe}}$, $(100)_\theta//(11\bar{1})_{\alpha\text{-Fe}}$, and $(03\bar{1})_\theta//(\bar{1}10)_{\alpha\text{-Fe}}$. Other SAED patterns, given in Figs. 5(e–g), can be simulated and explained by using the same logic, as shown in Figs. 6(j–l). The observed ORs (Fig. 5) are summarized in Table II, including Bagaryatsky OR[32] and Isaichev OR.[33] The small difference between Bagaryatsky and Isaichev ORs is indistinguishable in the TEM SAED patterns.[34]

TABLE I. Lattice parameters and structural information of the cementite phase.[28,29]

Orthorhombic Fe_3C	a(nm)	b(nm)	c(nm)	Fe-site	C-site
θ-Fe_3C	0.5092	0.6741	0.4527	0.03881, 1/4, 0.84222; 0.18347, 0.06897, 0.33448	0.87642, 1/4, 0.44262

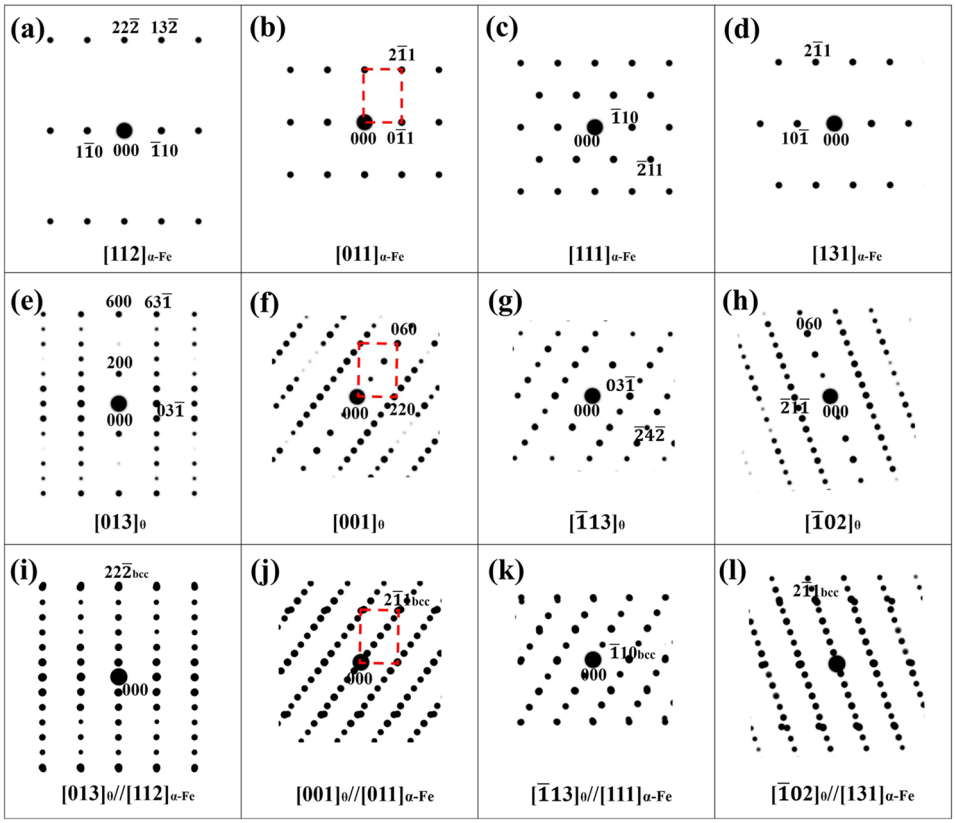

FIG. 6. (a-d) Calculated diffraction patterns of α-Fe along $[112]_{\alpha\text{-Fe}}$, $[011]_{\alpha\text{-Fe}}$, $[111]_{\alpha\text{-Fe}}$, and $[131]_{\alpha\text{-Fe}}$ ZAs, respectively; (e-h) calculated diffraction patterns of cementite (θ-Fe_3C) along $[301]_\theta$, $[100]_\theta$, $[3\bar{1}1]_\theta$, and $[2\bar{1}0]_\theta$ ZAs, respectively; and (i-l) simulated diffraction patterns to show the overlap between α-Fe and cementite along corresponding ZAs.

Due to the limitation of TEM tilting, if one ZA is observed, other ZAs will be confirmed during tilting of ferrite, such as $[011]_{\alpha\text{-Fe}}$ in $<110>_{\alpha\text{-Fe}}$, and cementite. The calculated pole diagrams of α-Fe and cementite are shown in Fig. 7 to validate ORs summarized in Table II. Figs. 7(a) and 7(b) show the pole diagrams taken along the $[112]_{\alpha\text{-Fe}}$ and $[013]_\theta$ direction-couple in Table II, whereas other direction-couples are marked in the pole diagrams. It is obvious that direction-couples match well with each other, except at very small angle differences. The above analysis confirmed that the θ-Fe_3C cementite formed during tempering and ORs indexed in Table II are reasonable.

The ω-Fe forms directly from face-centered cubic (fcc) austenite, and 12 ω-Fe variants could from at the same time by atomic shuffling or displacement.[35] During the transition of fcc to bcc, the ω-Fe can be treated as an intermediate stage[35,36] and assists in the formation of the bcc {112}<111>-type twin.[35] Simultaneously, the twinning boundary structure is also necessary to stabilize the ω-Fe(C) phase.[37] The ω-Fe phase is distributed at the twin boundary region as fine particles and the unit cell of the hexagonal ω-Fe phase has three iron atoms.[11,21–23] The theoretical calculation results have confirmed that carbon atoms can remain in the octahedral interstitial sites of ω-Fe particles.[21,37] After the addition of a carbon atom, the unit cell of ω-Fe phase exhibits the chemical composition of Fe_3C. The energy barrier for ω-Fe(C) to θ-Fe_3C transformation is quite small,[21] while the twin boundaries in martensite are suggested as the potent nucleation sites for carbides and cementite formation during tempering.[19,20] Therefore, ω-Fe particles with carbon atoms transformed into θ-Fe_3C cementite particles during tempering. In addition, the diffraction spots from the ω phase, located at 1/3 and 2/3 $(2\bar{1}1)_{\alpha\text{-Fe}}$ positions, overlapped with those from cementite during tempering, which implies that the ORs between newly generated cementite and

TABLE II. Orientation relationships (ORs) from TEM observations (Fig. 5).

Fig. 5(b)	Fig. 5(e)	Fig. 5(f)	Fig. 5(g)
$[013]_\theta//[112]_{\alpha\text{-Fe}}$	$[001]_\theta//[011]_{\alpha\text{-Fe}}$	$[\bar{1}13]_\theta//[111]_{\alpha\text{-Fe}}$	$[\bar{1}02]_\theta//[131]_{\alpha\text{-Fe}}$
$(100)_\theta//(11\bar{1})_{\alpha\text{-Fe}}$	$(220)_\theta//(0\bar{1}1)_{\alpha\text{-Fe}}$	$(03\bar{1})_\theta//(\bar{1}10)_{\alpha\text{-Fe}}$	$(010)_\theta//(2\bar{1}1)_{\alpha\text{-Fe}}$
$(03\bar{1})_\theta//(\bar{1}10)_{\alpha\text{-Fe}}$	$(010)_\theta//(2\bar{1}1)_{\alpha\text{-Fe}}$	$(\bar{1}2\bar{1})_\theta//(\bar{2}11)_{\alpha\text{-Fe}}$	$(\bar{2}1\bar{1})_\theta//(10\bar{1})_{\alpha\text{-Fe}}$

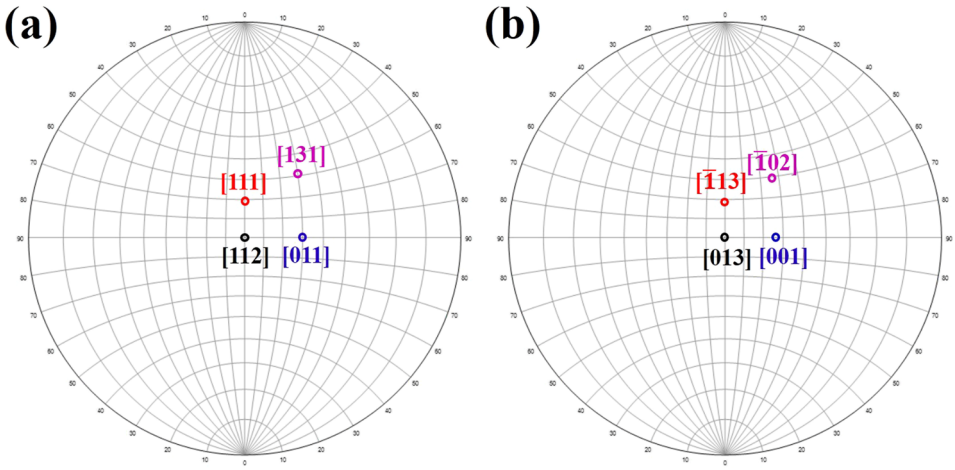

FIG. 7. Pole diagram of (a) α-Fe along [112] ZA and (b) cementite (θ-Fe_3C) along [301] ZA.

ferrite in tempered specimens can be related to ω-Fe to cementite transformation.

V. CONCLUSIONS

In summary, we have carried out detailed TEM and electron diffraction analysis of carbides formation in quenched and tempered high carbon steels. The diffraction spots, corresponding to θ-Fe_3C cementite, appeared at 1/6, 2/6, 3/6, 4/6 and 5/6 $(22\bar{2})_{\alpha\text{-Fe}}$ and $(2\bar{1}1)_{\alpha\text{-Fe}}$ positions along $[112]_{\alpha\text{-Fe}}$ and $[011]_{\alpha\text{-Fe}}$ zone axes during martensite tempering, whereas diffraction spots from the ω-Fe phase are located at 1/3 and 2/3 $(2\bar{1}1)_{\alpha\text{-Fe}}$ positions in martensite. The ω-Fe particles were observed at twin boundaries, which can be considered as a precursor for cementite and transformed into θ-Fe_3C cementite during tempering. Furthermore, orientation relationships between cementite and ferrite in the tempered specimen were indexed as $[013]_\theta//[112]_{\alpha\text{-Fe}}$, $[001]_\theta//[011]_{\alpha\text{-Fe}}$, $[\bar{1}13]_\theta//[111]_{\alpha\text{-Fe}}$ and $[\bar{1}02]_\theta//[131]_{\alpha\text{-Fe}}$. The observed orientation relationships between cementite and ferrite are related to the transformation of ω-Fe phase to θ-Fe_3C cementite.

ACKNOWLEDGMENTS

Financial support was provided by the Key Research Program of Frontier Sciences (Grant No. QYZDJSSW-JSC011) and the Strategic Priority Research Program of the Chinese Academy of Sciences (Grant No. XDB22040302).

REFERENCES

[1]G. Krauss, *Steels: Processing, Structure, and Performance* (ASM International, 2005).
[2]B. S. Lement, B. L. Averbach, and M. Cohen, "Microstructural changes on tempering iron-carbon alloys," Transactions of the ASM **46**, 851–877 (1954).
[3]F. Werner, B. Averbach, and M. Cohen, "The tempering of iron-carbon martensite crystals," Transactions of the ASM **49**, 823–841 (1957).
[4]T. Furuhara, K. Kobayashi, and T. Maki, "Control of cementite precipitation in lath martensite by rapid heating and tempering," ISIJ International **44**, 1937–1944 (2004).
[5]C. Revilla, B. López, and J. M. Rodriguez-Ibabe, "Carbide size refinement by controlling the heating rate during induction tempering in a low alloy steel," Materials & Design **62**, 296–304 (2014).
[6]V. K. Judge, J. G. Speer, K. D. Clarke, K. O. Findley, and A. J. Clarke, "Rapid thermal processing to enhance steel toughness," Scientific Reports **8**, 445 (2018).
[7]D. L. Williamson, K. Nakazawa, and G. Krauss, "A study on the early stages of tempering in an Fe-1.2C Pct alloy," Metallurgical Transactions A **10A**, 1351–1363 (1979).
[8]S. Nagakura, T. Suzuki, and M. Kusunoki, "Structure of the precipitated particles at the third stage of tempering of martensitic iron-carbon steel studied by high resolution electron microscopy," Transactions of the Japan Institute of Metals **22**, 699–709 (1981).
[9]A. J. Clarke, M. K. Miller, R. D. Field, D. R. Coughlin, P. J. Gibbs, K. D. Clarke, D. J. Alexander, K. A. Powers, P. A. Papin, and G. Krauss, "Atomic and nanoscale chemical and structural changes in quenched and tempered 4340 steel," Acta Materialia **77**, 17–27 (2014).
[10]D. T. Pierce, D. R. Coughlin, D. L. Williamson, K. D. Clarke, A. J. Clarke, J. G. Speer, and E. De Moor, "Characterization of transition carbides in quench and partitioned steel microstructures by Mössbauer spectroscopy and complementary techniques," Acta Materialia **90**, 417–430 (2015).
[11]D. H. Ping, T. W. Liu, M. Ohnuma, T. Ohmura, T. Abe, and H. Onodera, "Microstructural evolution and carbides in quenched ultra-low carbon (Fe–C) alloys," ISIJ International **57**, 1233–1240 (2017).
[12]X. Liu, T. H. Man, J. Yin, X. Lu, S. Q. Guo, T. Ohmura, and D. H. Ping, "In situ heating TEM observations on carbide formation and α-Fe recrystallization in twinned martensite," Scientific Reports **8**, 14454 (2018).
[13]E. M. Taleff, J. J. Lewandowski, and B. Pourladian, "Microstructure-property relationships in pearlitic eutectoid and hypereutectoid carbon steels," JOM **54**, 25–30 (2002).
[14]D. V. Edmonds and R. C. Cochrane, "Structure-property relationships in bainitic steels," Metallurgical Transactions A **21A**, 1527–1540 (1990).
[15]M. X. Zhang and P. M. Kelly, "Crystallography of spheroidite and tempered martensite," Acta Mater. **46**, 4081–4091 (1998).
[16]P. M. Kelly and J. Nutting, "The martensite transformation in carbon steels," Proc. Roy. Soc. A **259**, 45–58 (1960).
[17]A. G. Crocker, "Twinned martensite," Acta Metall. **10**, 113–122 (1962).
[18]A. B. Greninger, "Twinning in alpha iron," Nature **135**, 916–917 (1935).
[19]Y. Ohmori, "χ-carbide formation and its transformation into cementite during the tempering of martensite," Trans. JIM **13**, 119–127 (1972).
[20]M. G. H. Wells, "An electron transmission study of the tempering of martensite in an Fe-Ni-C alloys," Acta Metallurgica **12**, 389–399 (1964).
[21]D. H. Ping and W. T. Geng, "A popular metastable omega phase in body-centered cubic steels," Mater. Chem. Phys. **139**, 830–835 (2013).

[22]T. W. Liu, D. X. Zhang, Q. Liu, Y. J. Zheng, Y. J. Su, X. Q. Zhao, J. Yin, M. H. Song, and D. H. Ping, "A new nanoscale metastable iron phase in carbon steels," Scientific Reports **5**, 15331 (2015).
[23]T. W. Liu, D. H. Ping, T. Ohmura, and M. Ohnuma, "Electron diffraction analysis of quenched Fe–C martensite," J. Mater. Sci. **53**, 2976–2984 (2018).
[24]D. H. Ping and M. Ohnuma, "ω-Fe particle size and distribution in high-nitrogen martensitic steels," J. Mater. Sci. **53**, 5339–5355 (2018).
[25]T. H. Man, T. W. Liu, D. H. Ping, and T. Ohmura, "TEM investigations on lath martensite substructure in quenched Fe-0.2C alloys," Materials Characterization **135**, 175–182 (2018).
[26]X. Huang and N. H. Pryds, "Crystallography and morphology of cementite precipitates formed during rapid solidification of a ferritic stainless steel," Acta Mater. **48**, 4073–4082 (2000).
[27]K. W. Andrews, D. J. Dyson, and S. R. Keown, *Interpretation of Electron Diffraction Patterns* (Springer, New York, 1967).
[28]Z. Q. Lv, F. C. Zhang, S. H. Sun, Z. H. Wang, P. Jiang, W. H. Zhang, and W. T. Fu, "First-principles study on the mechanical, electronic and magnetic properties of Fe3C," Computational Materials Science **44**, 690–694 (2008).
[29]F. H. Herbstein and J. Smuts, "Comparison of X-ray and neutron-diffraction refinements of the structure of cementite Fe3C," Acta Cryst. **17**, 1331–1332 (1964).
[30]R. Bullough and C. M. Wayman, "Twinning and some associated diffraction effects in cubic and hexagonal metals: I-'selection rules' for twinning in fcc, bcc, and hcp lattice," Trans. TMS AIME **236**, 1704–1710 (1966).
[31]C. M. Wayman and R. Bullough, "Twinning and some associated diffraction effects in cubic and hexagonal metals: II-double diffraction," Trans. TMS AIME **236**, 1711–1715 (1966).
[32]Y. A. Bagaryatsky, "Likely mechanism for the tempering of martensite," Dokl. Akad. Nauk SSSR **73**, 1161–1164 (1950).
[33]I. V. Isaichev, "Orientation of cementite in tempered carbon steel," Zh. Tekh. Fiz. **17**, 835–838 (1947).
[34]D. S. Zhou and G. J. Shiflet, "Ferrite-cementite crystallography in pearlite," Metallurgical Transactions A **23A**, 1259–1269 (1992).
[35]D. H. Ping, "Understanding solid–solid (fcc-ω-bcc) transition at atomic scale," Acta Metall Sin (Engl. Lett.) **28**, 630–670 (2015).
[36]A. Togo and I. Tanaka, "Evolution of crystal structures in metallic elements," Phys. Rev. B **87**(184104), 1–6 (2013).
[37]Y. Ikeda and I. Tanaka, "ω structure in steel: A first-principle study," J. Alloys. Compd. **684**, 624–627 (2016).